

Article

# The Effect of Cerium Ions on the Structure, Porosity and Electrochemical Properties of Si/Zr-Based Hybrid Sol-Gel Coatings Deposited on Aluminum

Peter Rodič<sup>1</sup>, Jozefina Katić<sup>2</sup>, Dorota Korte<sup>3</sup>, Paula M. Desimone<sup>4</sup>, Mladen Franko<sup>3</sup>,  
Silvia M. Ceré<sup>4</sup>, Mirjana Metikoš-Huković<sup>2</sup> and Ingrid Milošev<sup>1,\*</sup> 

<sup>1</sup> Department of Physical and Organic Chemistry, Jožef Stefan Institute, Jamova c. 39, Ljubljana 1000, Slovenia; peter.rodic@ijs.si

<sup>2</sup> Department of Electrochemistry, Faculty of Chemical Engineering and Technology, University of Zagreb, Trg Marka Marulića 19, Zagreb 10000, Croatia; jkatic@fkit.hr (J.K.); mmetik@fkit.hr (M.M.-H.)

<sup>3</sup> Laboratory for Environmental and Life Sciences, University of Nova Gorica, Vipavska cesta 13, Nova Gorica 5000, Slovenia; Dorota.Korte@ung.si (D.K.); mladen.franko@ung.si (M.F.)

<sup>4</sup> Institute of Materials Science and Technology (INTEMA), University of Mar del Plata and National Research Council (CONICET), Av. J. B. Justo 4302, Mar del Plata 7600, Argentina; mdesimone@fi.mdp.edu.ar (P.M.D.); smcere@fi.mdp.edu.ar (S.M.C.)

\* Correspondence: ingrid.milosev@ijs.si; Tel.: +386-1-477-3452

Received: 12 February 2018; Accepted: 3 April 2018; Published: 7 April 2018



**Abstract:** This study was focused on the synthesis and characterization of Si/Zr-based hybrid sol-gel coatings with and without the addition of cerium(III) ions. The coatings were deposited on aluminum aiming to act as an effective and ecologically harmless alternative to toxic chromate coatings. The chemical composition, structure, thermal properties and porosity of the non-doped and Ce-doped coatings containing various Zr contents were examined by Raman spectroscopy and photothermal beam deflection spectroscopy. The corrosion properties of the coated aluminum substrates were studied using AC and DC electrochemical methods in 0.1 M NaCl electrolyte solution. Barrier and protecting properties of the coatings were monitored upon long-term immersion in chloride solution using electrochemical impedance spectroscopy. The effect of cerium ions was two-fold: on the formation of a more condensed Si–O–Zr network structure and on the formation of Ce-based deposits, which diminish the rate of cathodic reaction at the coating/metal interface. These effects acted synergistically and resulted in the creation of the coatings with effective barrier and active corrosion protection.

**Keywords:** aluminum; corrosion; hybrid sol-gel coatings; cerium nitrate; thermal properties; porosity

## 1. Introduction

Aluminum (Al >99.0%) is commonly used for numerous commercial applications due to its physical and chemical characteristics. However, in chloride solution, its corrosion resistance is limited because the passivity produced by the native protective aluminum oxide is susceptible to corrosion in aggressive environments [1]. In the past, hexavalent chromium-based compounds and chromate conversion coatings have been often used to inhibit corrosion processes [2,3], but stricter regulations have mandated that the usage of environmentally hazardous compounds must be reduced. Since September 2017, the use of chromates is banned or restricted in different industrial sectors [4]. The case is similar also for volatile organic compounds [5]. Therefore, the need exists for the development of non-toxic, environmentally-friendly surface treatments capable of providing sufficient corrosion protection. Today many studies are devoted to the development of pre-treatments

and coatings that would enable the replacement of hazardous chromates used hitherto in coating systems [6–8]. One of the promising alternatives is hybrid sol-gel coatings, which provide a physical barrier against water and penetration of aggressive ions to the metal [7,9]. Moreover, the sol-gel layer can be employed as an adhesion promotor with organic coatings [10]. Many organically-modified silicates (ormosils) demonstrated good anti-corrosion protection [11]. In addition, the inclusion of zirconium ions improves the anticorrosion properties of such coatings even further, due to the ability of consuming hydroxide ions at elevated pH, thereby protecting the silane matrix [12–15].

Hybrid Si/Zr coatings denoted as TMZ (based on tetraethyl orthosilicate (TEOS), 3-methacryloxy propyltrimethoxy silane (MAPTMS), zirconium tetrapropoxide (ZTP) and methacrylic acid (MAA)) have been investigated previously [12,16–18]. Synthesis, hydrolysis, condensation and polymerization reactions were studied in detail by different techniques such as FTIR, NMR, DLS, GDOES, AFM, SEM/EDS and TGA [12,16–18]. Amorphous, homogeneous coatings containing Si and Zr and polymerized organic matrix provide high corrosion resistance for aluminum [12] and aluminum alloys [19,20], even under aggressive conditions. The degree of protection is dependent on the Zr content in the coating, which stimulates the condensation reaction and formation of large domains of polycondensed Si species [12,18]. It affects the ageing and gelation reactions [12,18]. Consequently, the corrosion resistance of the coatings deposited on Al alloys is dependent on the Zr content; however, this dependence is not linear and must be optimized regarding other parameters such as ageing time and temperature, the presence of UV light, etc. [12,16–20]. In neutral chloride solutions, TMZ coatings containing a higher amount of ZTP expressed higher corrosion resistance [16].

The mechanical and corrosion coating properties of similar Si/Zr-based sol-gel systems have been investigated on aluminum alloys [18,20–23]. Such coatings present only barrier corrosion protection without active corrosion inhibition [18]. In order to improve this shortcoming, the addition of different species and compounds has been tested [24]. The most promising are inorganic/organic corrosion inhibitors added directly into the coating or added as nano-containers [25]. Rare earth cations, such as cerium(III) and cerium(IV) salts, were added in different hybrid sol-gel systems [26–28]. Cerium salts, e.g., chloride, acetate and nitrate, are recognized as efficient corrosion inhibitors for Al-based alloys when added directly in corrosive medium [29–31]. The inhibition mechanism is based on the formation of insoluble hydroxides,  $\text{Ce}(\text{OH})_3$  and  $\text{Ce}(\text{OH})_4$ , on the regions of the surface with local pH increase (up to 10.5) due to the cathodic reaction of oxygen reduction [32–34]. Therefore, in order to enable the hydroxide precipitation, the sol-gel coating itself needs to be resistant to elevated pH [13,35], which is indeed valid for the Si/Zr systems [12].

However, the addition of cerium salts into the sol-gel matrix changes its physical, chemical and corrosion properties [11,25]. Cerium is a network modifier, i.e., it increases the condensation rate of the hybrid sol and forms a more condensed network due to the reduction of the amount of silanol groups (Si–OH) [27,36]. The addition of cerium also leads to further condensation and crosslinking between polymer molecules [27,37,38]. Moreover, the cerium can migrate through the coating and improve the active corrosion protection, resulting in self-healing properties [28]. At the same time, it has to be assured that doping of the coating with cerium does not reduce the barrier properties of the coating, as cerium ions are bigger in size (1.978 Å) compared to silicon atoms (1.068 Å). The addition of the larger Ce amount might cause lattice deformation and the formation of nanopores and consequently dramatically change the characteristics of the coating [27,38].

The present work aims at producing hybrid TMZ sol-gel coatings with different amounts of zirconium tetrapropoxide with and without the addition of cerium ions to obtain better barrier, as well as active corrosion protection of aluminum. The addition of Ce ions to TMZ sols has not been studied yet. The coating composition, structure and porosity were characterized using Raman spectroscopy and photothermal beam deflection spectroscopy. The effect of the addition of cerium ions into the sol-gel matrix on the improvement of the corrosion performance was assessed by electrochemical techniques, especially after the longer exposure to corrosive NaCl medium. The Si/Zr sol-gel coatings were optimized by doping with  $\text{Ce}^{3+}$  ions that act as passivating/inhibiting agents of the system

metal | coating | aggressive environment. The concentration of Zr ions in the Si-Zr network structure plays the key role in the optimization of the system. Diffusivity of  $Ce^{3+}$  ions across the coating to the corrosion active sites on the metal substrate occurred without degradation of the coating's structural integrity. In addition, self-healing properties of the Ce-doped coatings were observed.

## 2. Materials and Methods

### 2.1. Materials and Chemicals

Aluminum (>99.0%), as a 1 mm-thick flat sheet, distributed by GoodFellow, England, was used as the substrate.

The chemicals used for sol-gel preparation were tetraethyl orthosilicate (TEOS:  $Si(OC_2H_5)_4$ , 99.9%, Aldrich, Munich, Germany), 3-methacryloxypropyltrimethoxysilane (MAPTMS:  $H_2C=C(CH_3)CO_2(CH_2)_3Si(OCH_3)_3$ ,  $\geq 98\%$ , Sigma, St. Louis, MO, USA), zirconium tetrapropoxide, (ZTP:  $Zr(OCH_2CH_2CH_3)_4$ , 70 wt. %, in 1-propanol, Aldrich, St. Louis, MO, USA), methacrylic acid (MAA:  $H_2C=C(CH_3)COOH$ , 99.0%, Aldrich, Zwijndrecht, The Netherlands) and hydrochloric acid (HCl, >37%, AppliChem, Darmstadt, Germany). The sols were doped with 0.5 wt% of cerium(III) nitrate hexahydrate ( $Ce(NO_3)_3 \cdot 6H_2O$ , 99.9%, Sigma, Lyon, France).

### 2.2. Synthesis of the Sols

Three different types of organic-inorganic hybrid systems were synthesized by mixing two separately prepared sols. The first silicon-based sol was prepared by mixing TEOS and MAPTMS, and the second sol, containing zirconium, was obtained by the addition of MAA to the ZTP. TEOS and MAPTMS were hydrolyzed under acidic conditions, combined with ZTP and MAA in order to provide the hybrid sol-gel solution, then stirred for one hour and aged for 2 days. The final sol is denoted as TMZ. The molar ratio of alkoxide precursors TEOS/MAPTMS/ZTP/MAA was 0.18:1:X:0.12, where X was 0.06, 0.12 and 0.48. The molar amounts of  $H_2O$  (2.075 mol) and catalyst HCl (0.001 mol) were kept constant. These sols/coatings are hereinafter referred to as TMZ-1, TMZ-2 and TMZ-3, respectively. TMZ-1 had the smallest and TMZ-3 the largest amount of ZTP. The preparation of TMZ sols was described in detail previously [17].

In the present work, the TMZ sols were further modified: 0.5 wt. % of  $Ce(NO_3)_3$  was added into sol, and the solution was vigorously stirred for 10 min. The clear sol was then aged for 1 h. Cerium-containing sols are denoted as TMZ-1-Ce, TMZ-2-Ce and TMZ-3-Ce, respectively.

### 2.3. Sample Preparation

The aluminum substrates were 1 mm-thick flat discs with a diameter of 15 mm. Before deposition, the substrate was ground under water with 2400- and 4000-grit SiC emery papers, rinsed with distilled water and cleaned in ethanol using an ultrasonic cleaner for 10 min. The aluminum alloy 7075-T6 (AA7075-T6) was also used as a substrate, because the bands in the Raman spectra were more clearly defined for coating deposited on this alloy due to a brighter surface.

The sol-gel coatings were applied on the aluminum surface using a spin-coater (WS-650-23NPP/LITE/IND, Laurell Technologies, Northwales, PA, USA). An excess amount of the sol was deposited on the substrate employing syringes equipped with filters (0.2  $\mu m$  pore size). The substrate was then rotated at 4000 rpm for 30 s in order to remove the excess sol and to facilitate the even coverage of the substrate. The coated samples were allowed to rest at ambient conditions for 10 min and were subsequently thermally cured by placement on a preheated hotplate at 100 °C for one hour in the presence of daylight.

The aforementioned procedure resulted in homogeneous, transparent, colorless and crack-free coatings with a thickness of approximately 3–4  $\mu m$  [12,16].

#### 2.4. Sample Characterization

Raman spectra were recorded on a Renishaw InVia Reflex confocal Raman microprobe (Gloucestershire, UK) with a Windows-based Raman Environment (version 3.1, Wire™, Gloucestershire, UK) software. A 785-nm diode laser with a nominal power of 300 mW was used as the excitation source, in combination with a grating of 1200 grooves/mm. The laser power was kept below 10% to avoid sample damage. A 50× (0.75 NA) Leica metallurgical objective was used in the excitation and collection paths. Spectra were typically acquired in 10 s with at least 3 accumulations at room temperature. Measurements were made in a Raman range extending from 200–3500 cm<sup>-1</sup>. The resolution of the spectra was better than 2 cm<sup>-1</sup>. Linear line 3D Raman analysis was performed in a region that was 40 μm wide and with a 5-μm step height.

Photothermal beam deflection (PBD) spectroscopy was employed to perform thermo-optical measurements to determine the ability of the material to exchange heat with the surroundings (defined by its thermal diffusivity ( $D_s$ )), as well as its ability to conduct the heat (defined by its conductivity ( $k_s$ )). These data were used to evaluate the coating porosity ( $P$ ).

The source of the pump beam, that is the He–Ne laser (632 nm, 35 mW) (MELLES GRIOT, Model 25-LHP-928-230, Carlsbad, Canada), heats the sample perpendicularly to its surface. The pump beam is an electro-optic amplitude modulator (New Focus, Model 4102-M, Newport, Irvine, CA, USA) at the output of which there is a polarizer (LPVIS100, Thorlabs, Munich, Germany). The light energy is absorbed by the sample and converted into heat that spreads into the surrounding medium (air) inducing temperature gradients (TGs) near the sample surface. A probe beam from another He–Ne laser (530 nm, 2 mW) (Uniphase, Model 1103P, Milpitas, CA, USA) passes through the TGs, skimming the sample's surface, thus changing its intensity, as recorded using a quadrant photodetector (RBM-R. Braumann GmbH, Model C30846E, Langenbach Kr. Freising, Germany) and lock-in amplifier (Stanford research instruments, Model SR830 DSP, Sunnyvale, CA, USA) connected to a PC.

The material's thermal properties ( $D_s$ ,  $k_s$ ) were evaluated by the use of a least-squares fitting procedure of the experimental data [39,40] collected in the form of the amplitude and phase dependence on the modulation frequency ( $f$ ) of the pump beam. During the fitting, the thermal conductivity and diffusivity were given trial values to get the best fit [41,42]. The fitting procedure was then repeated taking into account the materials' thermal properties by the relation describing their dependence on material porosity [15], Equation (1):

$$k_s = k_0 \frac{(\gamma + 2) + 2(\gamma - 1)P}{(\gamma + 2) - (\gamma - 1)P} \quad D_s = D_0 \frac{(\gamma + 2) + 2(\gamma - 1)P}{(1 + P)[(\gamma + 2) - (\gamma - 1)P]} \quad (1)$$

where  $\gamma$  is the ratio of the thermal conductivity of the cavities and material,  $P$  is the material's porosity,  $k_s$ ,  $D_s$  are the thermal conductivity and diffusivity of the porous material and  $k_0$ ,  $D_0$  are the thermal conductivity and diffusivity of the material without cavities, respectively. The fitted parameters were  $k_0$ ,  $D_0$  and  $P$ .

#### 2.5. Corrosion Evaluation

Electrochemical DC measurements were performed in a three-electrode standard corrosion cell (K00047 Corrosion Cell, volume 1 L, Ametek, Berwyn, PA, USA) at 25 °C. A specimen embedded in a Teflon holder, leaving an area of 0.785 cm<sup>2</sup> exposed to the solution, served as a working electrode. A silver/silver chloride electrode (Ag/AgCl, 0.205 V vs. saturated hydrogen electrode) was employed as the reference electrode and carbon rods as a counter electrode. Electrochemical experiments were carried out with a potentiostat/galvanostat (Metrohm Autolab, PGSTAT 12, Utrecht, The Netherlands) and controlled by Nova 1.11 software. Potentials in the text refer to the Ag/AgCl scale.

The corrosion performance of sol-gel coatings was evaluated under immersion in 0.1 M NaCl, pH = 5.5. The solution was prepared using Milli-Q Direct water with a resistivity of 18.2 MΩ·cm at 25 °C (Millipore, Billerica, MA, USA).

Prior to measurements, the sample was allowed to stabilize under open circuit conditions for approximately 1 h, to reach stable, quasi-steady state open circuit potential ( $E_{oc}$ ) at the end of the stabilization period. Following stabilization, the electrochemical measurements were carried out. First, the linear polarization measurements were performed in a potential range of  $\pm 10$  mV vs. stable  $E_{oc}$ , using a 0.1 mV/s potential scan rate. The values of polarization resistance ( $R_p$ ) were deduced from the slope of fitted current density vs. potential lines using Nova software. Then, the potentiodynamic polarization measurements were performed using a 1 mV/s potential scan rate, starting from  $-250$  mV to stable  $E_{oc}$  and then increased in the anodic direction. For each sample, measurements were performed at least in triplicate, and the representative measurement was chosen to be presented in graphs. In the tables, the results are presented as the mean  $\pm$  standard deviation. Corrosion potential ( $E_{corr}$ ) and corrosion current density ( $j_{corr}$ ) were obtained from an intercept between the cathodic and anodic curves.

The barrier (electric and dielectric) properties of the hybrid coating based on Si and Zr deposited on aluminum were investigated at the  $E_{oc}$  using electrochemical impedance spectroscopy (EIS). EIS measurements were performed in a three-electrode cell (K0235 Flat Cell Kit, volume 250 mL Ametek, Berwyn, PA, USA) at 25 °C. A specimen embedded in a Teflon holder, leaving an area of 1.0 cm<sup>2</sup> exposed to the solution, served as a working electrode. A silver/silver chloride (Ag/AgCl, 0.205 V vs. saturated hydrogen electrode) was used as the reference electrode and platinum mesh as a counter electrode. Potentials in the text refer to the Ag/AgCl scale. Measurements were performed in the frequency range from 100 kHz–10 mHz at an AC voltage amplitude of  $\pm 10$  mV (Metrohm Autolab, PGSTAT 12, Utrecht, The Netherlands). The experimental data were fitted using the complex non-linear least squares (CNLS) fit analysis software [43], and values of the elements of the proposed electric equivalent circuit (EEC) were derived with  $\chi^2$  values less than  $3 \times 10^{-3}$  (errors in parameter values of 1–5%) using ZView<sup>®</sup> software (version 3.5c, Southern Pines, NC, USA).

Since the frequency dispersion is present, the capacitor in EEC was replaced with the constant phase element (CPE). The impedance of CPE is defined as  $Z(\text{CPE}) = [Q(j\omega)^n]^{-1}$ , where  $j\omega$  is the complex variable and  $n$  is the exponent of CPE, while  $Q$  is the frequency-independent parameter of the CPE, which represents a pure capacitance when  $n = 1$  [44–46].

### 3. Results

#### 3.1. Composition and Structure of Hybrid Coatings

Raman spectroscopy is a powerful and versatile research technique for the analysis of the composition and structure of the TMZ sol-gel coatings, as well as monitoring their changes upon different Zr content and Ce-doping. Three main objectives of the Raman measurements were: (i) to compare the spectra for coatings with different amounts of ZTP (TMZ-1, TMZ-2, TMZ-3) and determine the influence of zirconium content on the coating composition; (ii) to determine the homogeneity of the TMZ-3 coating using line scanning and (iii) to compare the spectra for non-doped (TMZ-3) and doped (TMZ-3-Ce) coatings in order to determine the influence of cerium addition on the coating structure.

The Raman spectra recorded for TMZ-1, TMZ-2 and TMZ-3 coatings in the range from 200–1800 cm<sup>-1</sup> are presented in Figure 1. The spectra also contain strong Raman bands between 2850 cm<sup>-1</sup> and 2980 cm<sup>-1</sup> assigned to C–H stretching (not shown in Figure 1).

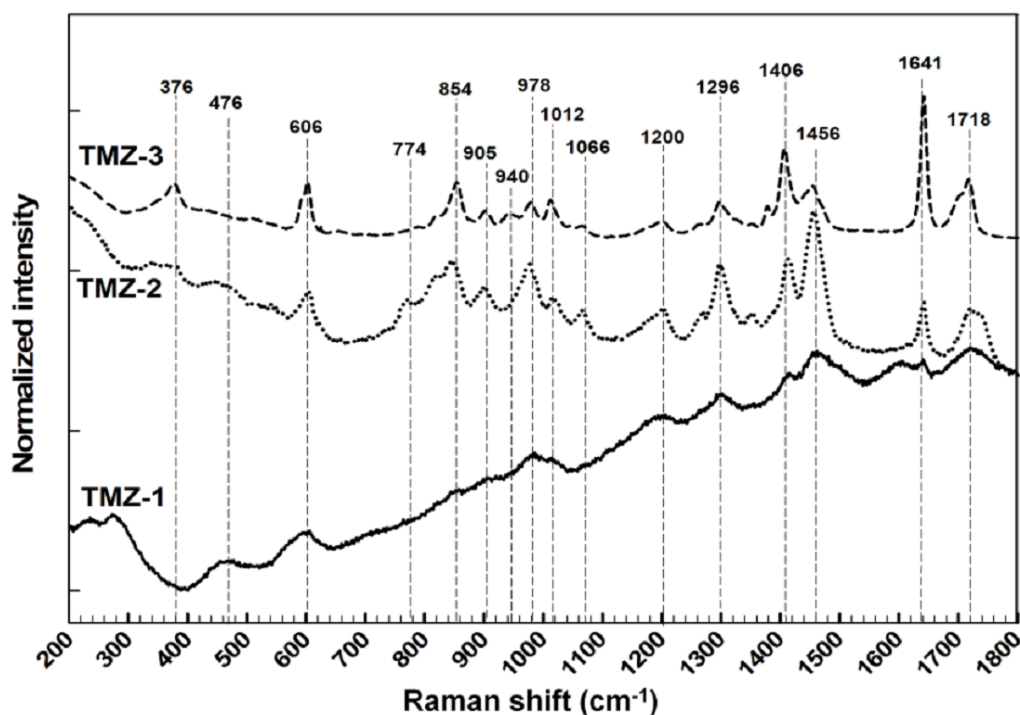


Figure 1. Raman spectra recorded for the TMZ-1, TMZ-2 and TMZ-3 coatings.

The resolution of the spectra for TMZ-1 is lower compared to that for the TMZ-2 and TMZ-3 coatings, which is related to the difference in the coating structure, reflecting the difference in optical properties [12] and consequently also the quality of the Raman signal. Spectra for TMZ-2 and TMZ-3 are more similar, but there are differences between some characteristic bands indicating different coating structures. These bands correspond to symmetric silicon-oxygen stretching vibrations of silicate tetrahedral units, corresponding to  $\text{SiO}_4$ ,  $-\text{SiO}_3$ ,  $-\text{SiO}_2$  and  $-\text{SiO}$  non-bridging oxygen atoms, which appear in the Raman spectrum of silicate at the  $\sim 850$ ,  $\sim 900$ ,  $950\text{--}1000$  and  $1050\text{--}1100\text{ cm}^{-1}$  positions, respectively [47]. Therefore, changes in the ratio between bands at  $978$  and  $1012\text{ cm}^{-1}$  are related to changes in the structure. The TMZ-3 coating presents a lower amount of non-bridging and a higher amount of bridging oxygen on the silicon atom compared to TMZ-2.

The bands between  $950\text{ cm}^{-1}$  and  $1100\text{ cm}^{-1}$  are assigned to the asymmetric stretching of  $\text{Si-O-Zr}$  groups [16,17]. This confirms that during the condensation reaction, a siloxane structure is formed. The related band is located at  $978\text{ cm}^{-1}$  and can be assigned to the vibrational mode involving  $\text{Si-O-Zr}$  linkages. The intensity of the band increases with the ZTP concentration in the coating.

Bands at  $1718\text{ cm}^{-1}$  and  $1705\text{ cm}^{-1}$  are due to stretching modes of  $\text{C=O}$  groups, which interact with  $\text{C=C}$  at  $1641\text{ cm}^{-1}$ . Bands at  $1456\text{ cm}^{-1}$  and  $1370\text{ cm}^{-1}$  are due to symmetric and asymmetric bending modes of  $-\text{CH}_2$  and  $-\text{CH}$  groups of organically-modified silicon in MAPTMS. Strong bands at  $854\text{ cm}^{-1}$  and  $376\text{ cm}^{-1}$  can be assigned to  $\text{C-C-O}$  and  $\text{C-O-C}$  stretching in MAPTMS. A broad band at  $\sim 476\text{ cm}^{-1}$  and a sharp band at  $606\text{ cm}^{-1}$  have been associated with breathing vibrations of oxygen atoms in four- and three-membered rings, respectively [48].

The spectrum for the TMZ-3 coating has additional bands at  $1378\text{ cm}^{-1}$  and  $940\text{ cm}^{-1}$  (the band is overlapping with the band for  $\text{Si-OH}$ ), which can be associated with higher zirconium content and the formation  $\text{Zr-O-Zr}$  and  $\text{Si-O-Zr}$  bonds. The band at  $940\text{ cm}^{-1}$  is associated with the  $\text{Si-OH}$  stretching of non-condensed species present in the coating. These bands are present even after thermal curing, confirming that the polymerization was not completed under these conditions. The characteristic Raman bands for  $\text{ZrO}_2$  are located around  $470\text{ cm}^{-1}$ ,  $620\text{ cm}^{-1}$  and  $650\text{ cm}^{-1}$ , but these bands are not observed in the obtained spectra. This rules out the formation of  $\text{ZrO}_2$ , which

was in the literature reported as the reason for more effective corrosion protection of Zr-based sol-gel coatings [14,49]. As the Raman technique has a relatively high resolution, the possibility of  $\text{ZrO}_2$  formation can be excluded.

Raman spectroscopy was also employed to check for the homogeneity of the TMZ coatings. As a representative, the spectra for the TMZ-3 coating are shown in Figure A1. The spectra confirm a high homogeneity along the 40  $\mu\text{m}$ -long analyzed line of the coating. All spectra have the characteristic bands described above at the same position with similar intensity.

Raman spectra for the TMZ-3 and TMZ-3-Ce coatings are shown in Figure 2. The most important feature is the intensity decrease in the band at  $940\text{ cm}^{-1}$  and the appearance of a new band at  $956\text{ cm}^{-1}$ , confirming a higher condensation degree of TMZ-3-Ce. The ratio between bands at 978 and  $1012\text{ cm}^{-1}$  is changed (the intensity of the band at  $978\text{ cm}^{-1}$  is higher), confirming the incorporation of cerium into the coating structure. It seems that the non-condensed species were replaced by cerium ions, and consequently, more species with two oxygen bridges and silicon were formed.

Cerium dioxide has a fluorite structure. Typical Raman band around  $460\text{ cm}^{-1}$  refers to an  $\text{F}_{2g}$  triply-degenerated vibrational mode. The  $\text{F}_{2g}$  mode can be related to the first-order Raman active mode of  $\text{CeO}_2$ , which can be viewed as the expansion and contraction of the eight oxygen anions around each cerium cation in the crystalline structure [50,51]. According to the literature, the cerium is in the coating present as  $\text{Ce}^{3+}$  and  $\text{Ce}^{4+}$ , because during the preparation (mixing and thermal curing) of TMZ sols,  $\text{Ce}^{3+}$  can be oxidized to  $\text{Ce}^{4+}$ . Both valences are present in the coating as the oxidation is not completed [27,52]. Due to the presence of both oxidation states, the Raman peak is shifted to the lower wavenumbers, i.e., to  $444\text{ cm}^{-1}$ , and is associated with vibrations in the structure considered as the symmetric stretching mode of oxygen atoms around cerium ions. Both oxidation states of cerium act as corrosion inhibitors [53]. The band for the Si–OH group at  $940\text{ cm}^{-1}$  disappeared confirming the formation of a more condensed Si–O–Si structure. The spectra of the line scanning of the TMZ-3-Ce coating with 0.5 wt. %  $\text{Ce}(\text{NO}_3)_3$  are shown in Figure A2. Spectra confirm the homogeneity throughout the coating and indicate that cerium is homogeneously integrated in the coating structure and forms the network with Si and Zr.

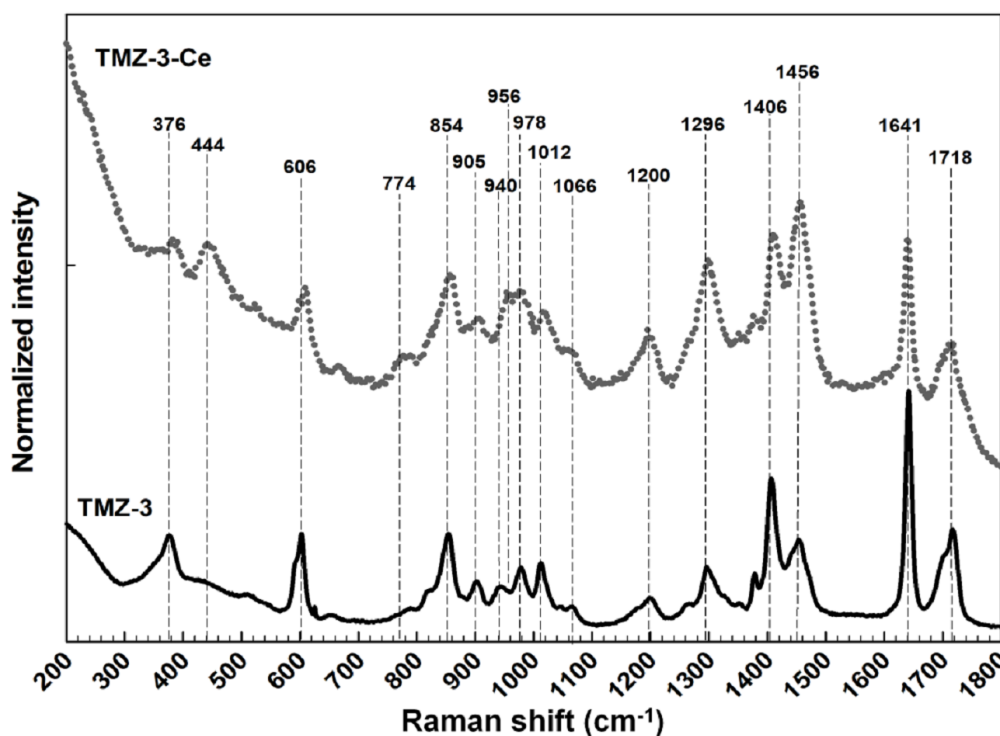


Figure 2. Raman spectra obtained for non-doped TMZ and Ce-doped TMZ-3-Ce coating.

### 3.2. Thermal Properties

The efficient barrier corrosion protection is often related to the high coating density and low porosity. To obtain this information, the porosity values deduced from thermal properties were evaluated for TMZ and TMZ-Ce coatings. The thermal conductivity,  $k_s$ , and thermal diffusivity,  $D_s$ , along with the deduced porosity,  $P$ , of the non-doped and Ce-doped TMZ coatings are given in Table 1.

**Table 1.** Thermal parameters determined using photothermal beam deflection spectroscopy: thermal diffusivity,  $D_s$ , thermal conductivity,  $k_s$ , and calculated porosity,  $P$ , of the non-doped and Ce-doped TMZ coatings.

Material/Coating	$D_s \times 10^{-7}$ (m <sup>2</sup> /s)	$P$ (%)	$k_s$ (W/(m·K))	$P$ (%)
TMZ-1	2.53	0.96	0.26	0.85
TMZ-2	2.44	0.85	0.25	0.78
TMZ-3	2.05	0.58	0.21	0.49
TMZ-1 + Ce(NO <sub>3</sub> ) <sub>3</sub>	2.14	0.88	0.22	0.73
TMZ-2 + Ce(NO <sub>3</sub> ) <sub>3</sub>	1.96	0.76	0.20	0.67
TMZ-3 + Ce(NO <sub>3</sub> ) <sub>3</sub>	1.75	0.51	0.18	0.42

Different amounts of zirconium in the siloxane network and the addition of cerium ions into Si/Zr sol are reflected in the different thermal properties. The differences in their thermal parameters are attributed to the difference in the structure and nano-organization of the Si/Zr structure. Zirconium is incorporated in the siloxane structure, which makes the material more compact. Consequently, thermal conductivity and diffusivity decrease with increasing amount of zirconium in the coating (from TMZ-1–TMZ-3) which causes an increase in the material's thermal resistance and is not compensated by the decrease in the coating porosity. Reduced  $D_s$  and  $k_s$  values imply lower porosity of the coating, which decreased from 0.85–0.49% from the TMZ-1–TMZ-3 coating (calculated from  $k_s$ ).

The addition of cerium ions into the TMZ coating leads to an even more condensed network structure (Figure 2) and, consequently, further affects the thermal parameters of the coatings. The  $D_s$  and  $k_s$  values are reduced showing the minimum porosity value for the TMZ-3-Ce coating (0.42%). This confirms that the addition of cerium ions contributes to a lower porosity and thus improves the barrier properties of the coating.

### 3.3. Electrochemical Characterization

#### 3.3.1. DC Electrochemical Tests

The corrosion properties of uncoated Al and TMZ and TMZ-Ce coated Al were firstly evaluated in 0.1 M NaCl solution using linear polarization and potentiodynamic polarization techniques (Table 2 and Figure 3a,b). Values of polarization resistance,  $R_p$ , deduced at the  $E_{oc}$ , differ substantially between uncoated and coated samples (Table 2). With increasing content of Zr in the coating, the  $R_p$  values increased almost two-fold. The addition of Ce to the TMZ coatings further increased the  $R_p$  values, indicating improved resistance of aluminum to general corrosion. The highest  $R_p$  value was obtained for the TMZ-3-Ce coating.

**Table 2.** Polarization resistance,  $R_p$ , corrosion potential,  $E_{\text{corr}}$ , and corrosion current density,  $j_{\text{corr}}$ , measured in 0.1 M NaCl for uncoated and TMZ- and TMZ-Ce-coated aluminum after 1 h of stabilization at the open circuit potential. Results are presented as the mean value  $\pm$  the standard deviation.

Material/Coating	$R_p$ ( $M\Omega \cdot \text{cm}^2$ )	$E_{\text{corr}}$ (V)	$j_{\text{corr}}$ ( $\text{nA}/\text{cm}^2$ )
Aluminum	$0.013 \pm 0.002$	$-0.75 \pm 0.02$	$296 \pm 40$
TMZ-1	$7.7 \pm 1.4$	$-0.69 \pm 0.03$	$5.4 \pm 0.2$
TMZ-2	$11.8 \pm 2.1$	$-0.68 \pm 0.02$	$4.1 \pm 0.2$
TMZ-3	$14.1 \pm 2.4$	$-0.65 \pm 0.02$	$2.9 \pm 0.1$
TMZ-1-Ce	$8.4 \pm 1.7$	$-0.68 \pm 0.02$	$3.0 \pm 0.2$
TMZ-2-Ce	$18.7 \pm 2.5$	$-0.70 \pm 0.02$	$2.2 \pm 0.1$
TMZ-3-Ce	$30.4 \pm 2.8$	$-0.62 \pm 0.03$	$1.2 \pm 0.1$

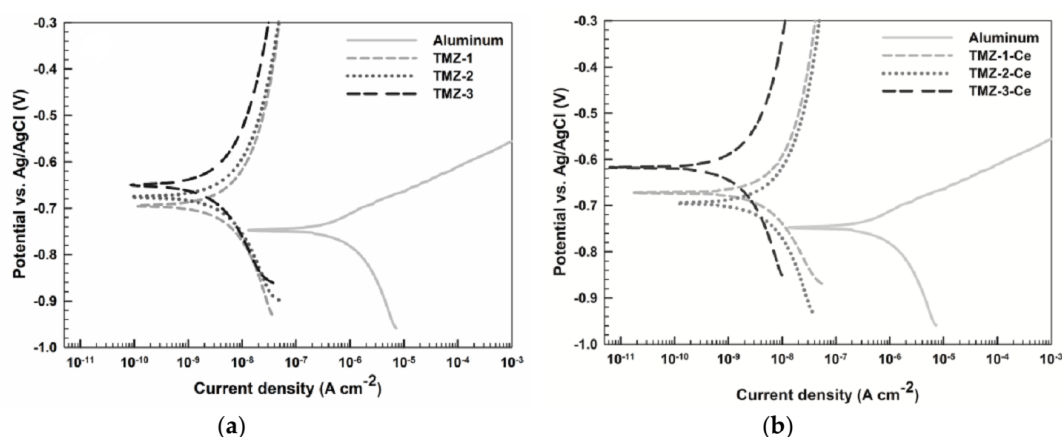


**Figure 3.** Potentiodynamic polarization curves recorded in 0.1 M NaCl for uncoated aluminum and aluminum coated with (a) non-doped TMZ coating and (b) Ce-doped TMZ-Ce coatings.  $dE/dt = 1 \text{ mV/s}$ .

The shape of the curves of the uncoated aluminum significantly differs from that of TMZ-coated aluminum indicating greatly improved corrosion protection achieved by the coatings (Figure 3a). The corrosion current density values,  $j_{\text{corr}}$ , are reduced by two orders of magnitude, and  $E_{\text{corr}}$  values are shifted to the more positive potentials (Table 2). The  $j_{\text{corr}}$  decrease follows the increasing Zr content in the coating, indicating that the additional presence of Si–O–Zr groups (Figure 1) beneficially affects the corrosion properties.

The corrosion properties were further improved for the TMZ coatings doped with cerium ions. The TMZ-Ce coatings showed a  $j_{\text{corr}}$  decrease down to values four orders of magnitude lower compared to uncoated aluminum and several times lower compared to TMZ coatings. From the results of the polarization measurements, it can be concluded that the addition of Ce ions to the TMZ coating acts beneficially on the coating's corrosion performance.

### 3.3.2. Long-Term Corrosion Tests

Since Si/Zr hybrid sol-gel coatings with the highest Zr content showed improved corrosion properties during preliminary DC electrochemical tests, further investigations were performed only on TMZ-3 coatings (non-doped and Ce-doped). Special attention was given to the study of the long-lasting anticorrosive protection properties of these coatings.

Figure 4 depicts the dependence of  $E_{\text{oc}}$  on the immersion time for the TMZ-3 and TMZ-3-Ce coatings. Upon immersion of the TMZ-3 coating,  $E_{\text{oc}}$  was ca.  $-0.58 \text{ V}$  and then shifted in a more positive direction reaching  $-0.42 \text{ V}$  after approximately nine days. However, at longer immersion times, the values shifted to more negative values, due to the progressive degradation of TMZ coating. On the other hand, for the TMZ-3-Ce coating,  $E_{\text{oc}}$  remained more positive and did not shift in the

negative direction. This behavior may be the consequence of cerium ions in the coating, which increase the barrier effect, but may also contribute to the self-healing effect [54], as will be discussed later.

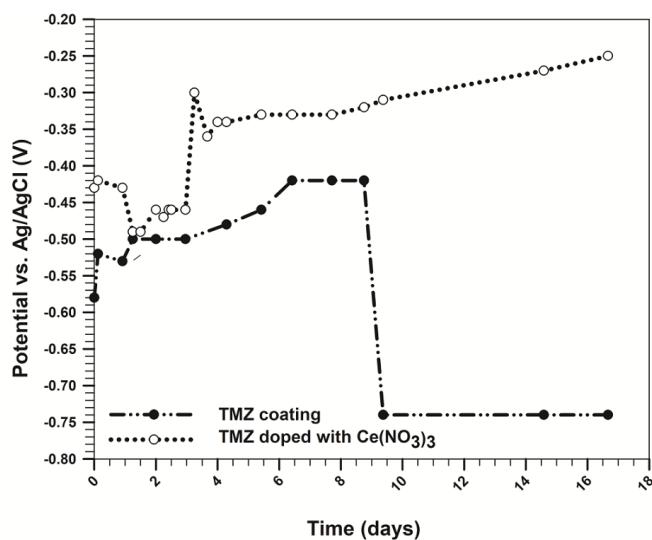


**Figure 4.** The dependence of open circuit potential ( $E_{oc}$ ) on the immersion time in 0.1 M NaCl for TMZ-3 and TMZ-3-Ce coatings.

Barrier properties of TMZ-3 and TMZ-3-Ce coatings during immersion in the corrosive media were investigated using electrochemical impedance spectroscopy. EIS, as a useful and reliable in situ nondestructive method, enabled the determination of the charge and potential distribution at the metal | coating and coating | electrolyte interfaces.

The impedance spectra of TMZ-3 and TMZ-3-Ce coatings were recorded in 0.1 M NaCl solution and are presented in the form of Bode plots in Figures 5 and 6, respectively. The measurements were performed at different immersion times at the  $E_{oc}$  representing real application conditions of Al coated samples in an electrolyte solution.

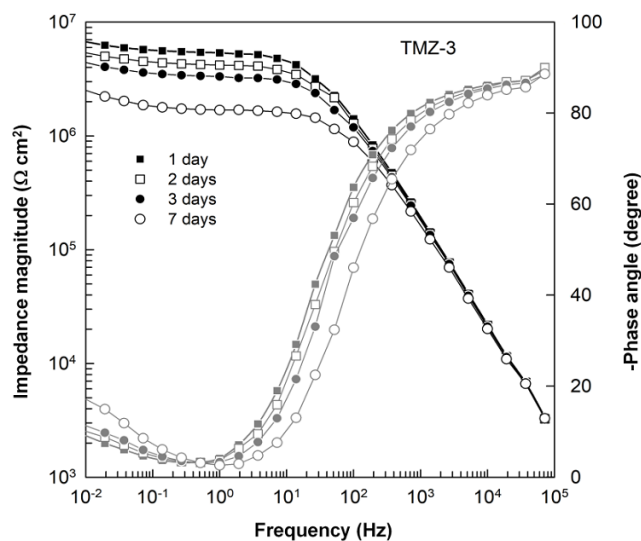


**Figure 5.** Bode plots for the TMZ-3 coating deposited on aluminum recorded at the open circuit potential in 0.1 M NaCl solution after the different immersion times denoted. Symbols correspond to experimental data and lines to the fitted data.

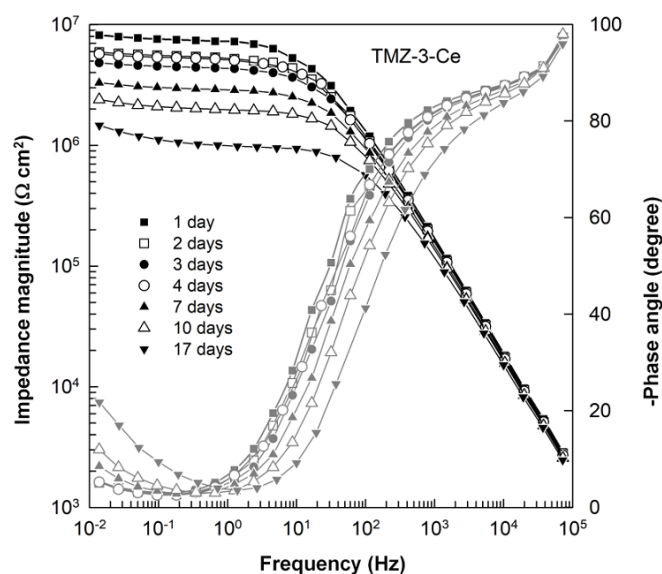


**Figure 6.** Bode plots for the Ce-doped coating (TMZ-3-Ce) deposited on aluminum and recorded at the open circuit potential in 0.1 M NaCl solution at different immersion times denoted. Symbols correspond to experimental data and lines to the fitted data.

Both sol-gel prepared coatings, TMZ-3 and TMZ-3-Ce, show phase angle values close to  $-90^\circ$ , stretching over high frequency range, which indicate the highly capacitive character of the coatings. The impedance magnitude values,  $|Z|$ , reached a plateau at frequencies lower than 10 Hz associated with the contribution of the corrosion resistance of the coated metal substrate in contact with the aggressive environment (NaCl solution). Upon the immersion, the impedance magnitude values slightly decreased, and the phase angle values shifted to the higher frequencies. These changes point to the progressive development of corrosion processes in the investigated systems. However, the extent of the impedance plateaus remained unchanged, indicating that the degradation processes did not significantly affect the coatings' structure and, in turn, the corrosion rate of the underlying Al substrate. For example, the  $|Z|$  values of Al coated samples TMZ-3 and TMZ-3-Ce are in the range of a few  $M\Omega\text{ cm}^2$  after an immersion time of seven days. This clearly confirms that the Si/Zr-based hybrid sol-gel coatings impart good corrosion resistance and represent an effective anticorrosion barrier for the underlying Al substrate. Moreover, the  $|Z|$  values persisted at these high values even after prolonged immersion up to 17 days.

The EIS results for the coated Al substrates, Figures 5 and 6, are interpreted based on the two-layer coating model consisting of an inner layer composed of natural aluminum oxide and the outer Si/Zr-based hybrid coating prepared with or without the addition of  $\text{Ce}(\text{NO}_3)_3$  salt (Figure 7).

The impedance data for TMZ-3 and TMZ-3-Ce coatings were fitted using CNLS fit analysis software, as described in the Materials and Methods section. EEC with three time constants, which are clearly resolved in the Bode plots for all immersion times, was employed (Figure 7), and the corresponding EEC parameter values are listed in Table 3. The quality of the impedance fit was characterized with  $\chi^2$  values less than  $3 \times 10^{-3}$  and errors in single EEC parameter values of 1–5%.

The  $R_{\text{coat}}$  and  $Q_{\text{coat}}$  parameters represent the coating resistance and the pseudo-capacitance of the film|electrolyte interface. The  $R_{\text{oxide}}$  and  $Q_{\text{oxide}}$  parameters ascribe the resistance and pseudo-capacitance of the intermediate oxide layer. The  $Q_{\text{dl}}$  is the double layer interfacial capacitance and the  $R_{\text{ct}}$  parameter is the charge-transfer resistance describing the Faradaic reaction at the metal|electrolyte solution interface occurring as a result of structure defects in the sol-gel coating upon immersion in NaCl solution. The sum of the  $R_{\text{oxide}}$  and  $R_{\text{ct}}$  parameters is equal to the polarization

resistance,  $R_p$ , which reflects the corrosion rate of the aluminum substrate according to the theory of the kinetics for corrosion processes at the metal | electrolyte solution interface [55].

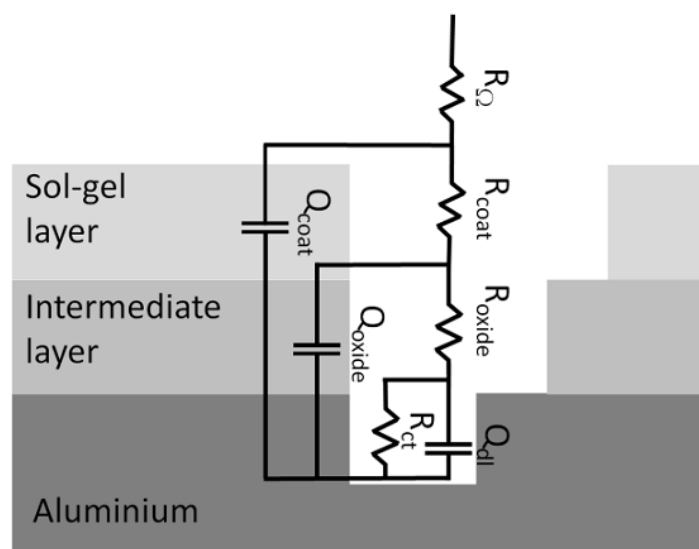


**Figure 7.** The electric equivalent circuit (EEC) used for numerical fitting of the EIS data of the coated aluminum.

The  $R_p$  values of TMZ-3 and TMZ-3-Ce coatings are equal to  $12 \text{ M}\Omega \text{ cm}^2$  and  $33 \text{ M}\Omega \text{ cm}^2$  after the immersion time of 1 h, respectively (impedance spectra not shown). It should be stressed that the  $R_p$  values, given in Table 2, obtained from DC measurements (linear polarization method) are in good agreement with the  $R_p$  values obtained from AC measurements (EIS data) after the immersion time of one hour. In the theory of corrosion kinetics, the value of the  $R_p$  would be the most appropriate parameter for monitoring the protective properties of the coating as the corrosion rate of the underlying metal is under the charge transfer control and can be estimated from the Mansfeld–Oldham relation [56].

As can be seen from the impedance parameters obtained (Table 3),  $R_{\text{coat}}$  values are changed depending on the Ce-doping of the TMZ-3 coatings. The observed  $R_{\text{coat}}$  values decrease during prolonged immersion time (Figure 8a), suggesting the formation of the pores (defects) in the Si/Zr-based hybrid layer. Actually, these pores facilitated  $\text{Ce}^{3+}$  ions transfer/migration within the layer [28]. Nevertheless, the high  $n_{\text{coat}}$  and low  $Q_{\text{coat}}$  values point to the presence of the compact coating layer, which is additionally supported by the underlying intermediate oxide layer. Thus, although the  $R_{\text{coat}}$  changed upon Ce-doping, the coating's barrier properties ( $R_p$ ) were not significantly affected during the immersion of the sample in the aggressive environment. The beneficial effect of the Ce-doping is confirmed by the increase in  $R_{\text{oxide}}$  values, which is more pronounced for the longer times of immersion. Subsequently, the  $R_p$  parameter of the TMZ-3-Ce coating shows higher values in comparison to that of the TMZ-3 coating (Figure 8b). This can be explained by the stimulation of the condensation processes of the matrix, i.e., the facilitated production of stable Si–O–Si and Si–O–Zr network structure with ZTP-MAA coordination and the intermediate oxide layer due to the presence of cerium as a network modifier. Hence, the addition of  $\text{Ce}^{3+}$  ions increases the Al–O–Si/Zr bond density across the substrate | coating interface and enhances the compactness of the resulted intermediate layer [24,33]. This is in accordance with the Raman spectroscopy and PBD spectroscopy results, confirming the formation of TMZ-Ce coatings with microstructural homogeneity, good internal cohesion and decreased porosity.

The impedance in the lowest frequency range was related to the corrosion process at the metal | electrolyte interface under a charge-transfer control described by  $R_{\text{ct}}$  parameter values. The TMZ

coating maintains high and nearly constant  $R_{ct}$  values during an immersion time of seven days. However, the drop in the overall coating's resistance parameter,  $R_p$  (Figure 8b), suggests that the initiation of the pitting cannot be stopped due to the absence of a corrosion inhibitor in the coating. According to Table 3, both parameters for the Ce-doped coating,  $R_{ct}$  and  $Q_{dl}$ , indicate the presence of deposits at the metal | electrolyte interface due the release of  $Ce^{3+}$  ions from the hybrid coating structure upon immersion and the increase of ionic conductivity during deposit formation. Precipitation of cerium oxide/hydroxide occurs on the corrosion active sites of the Al substrate and induces the inhibiting effect, as was discussed before [28,57,58]. Hence, due to the corrosion processes occurring at the metal | electrolyte interface, the ionic conductivity rises, which is reflected in the decrease of the  $R_{ct}$  values for the TMZ-3-Ce coating.

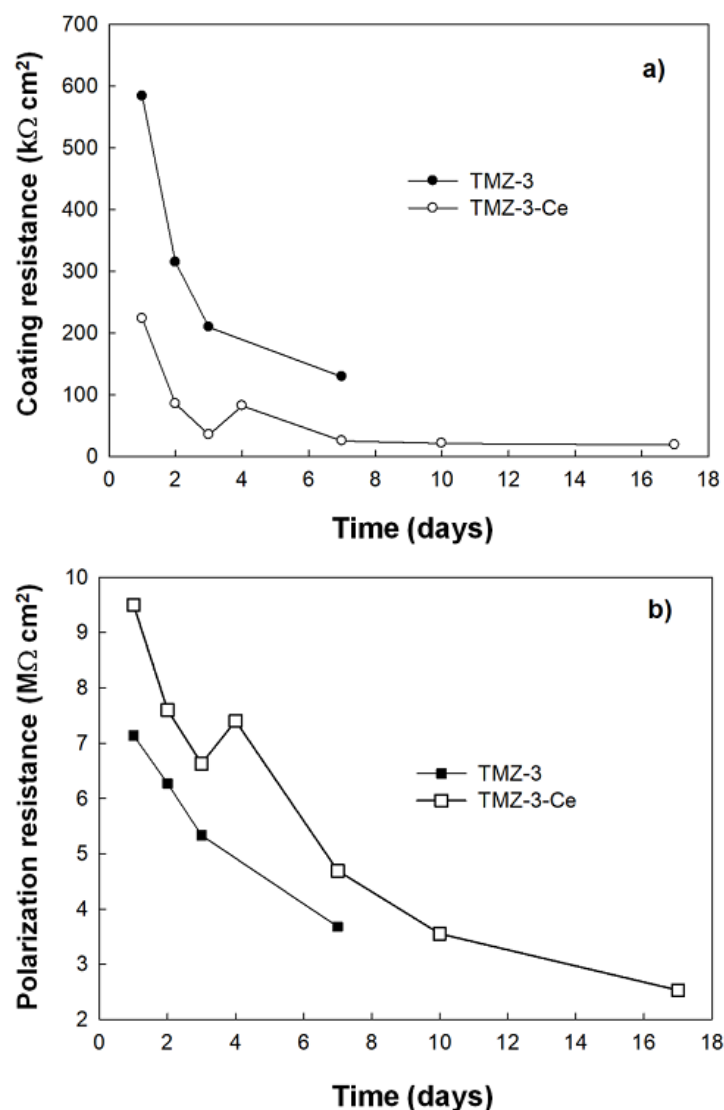


**Figure 8.** (a) The coating resistance ( $R_{coat}$ ) and (b) the polarization resistance ( $R_p$ ) for non-doped TMZ-3 and Ce-doped TMZ-3-Ce coatings deposited on aluminum as a function of immersion time in 0.1 M NaCl.

**Table 3.** Impedance parameters of the Si/Zr-based hybrid non-doped (TMZ-3) and Ce-doped (TMZ-3-Ce) coatings deposited on aluminum recorded at the open circuit potential,  $E_{oc}$ , in 0.1 M NaCl solution after the different immersion times.  $R_{\Omega} = 23 \Omega \text{ cm}^2$

Immersion time	$Q_{coat} \times 10^9$ ( $\Omega^{-1} \text{ cm}^{-2} \text{ s}^n$ )	$n_{coat}$	$R_{coat}$ ( $\text{k}\Omega \text{ cm}^2$ )	$Q_{oxide} \times 10^9$ ( $\Omega^{-1} \text{ cm}^{-2} \text{ s}^n$ )	$n_{oxide}$	$R_{oxide}$ ( $\text{M}\Omega \text{ cm}^2$ )	$Q_{dl} \times 10^6$ ( $\Omega^{-1} \text{ cm}^{-2} \text{ s}^n$ )	$n_{dl}$	$R_{ct}$ ( $\text{M}\Omega \text{ cm}^2$ )
TMZ-3									
1 day	0.93	0.974	583.1	3.84	0.642	5.02	5.08	0.894	2.12
2 days	0.86	0.982	314.3	4.02	0.659	4.03	4.16	0.830	2.24
3 days	0.93	0.974	209.1	4.32	0.652	3.22	5.06	0.821	2.11
7 days	0.92	0.977	129.2	5.04	0.682	1.58	6.22	0.790	2.10
TMZ-3-Ce									
1 day	0.84	0.997	223.2	4.74	0.621	7.42	6.82	0.825	2.08
2 days	0.85	0.996	85.3	5.61	0.609	5.53	11.30	0.830	2.07
3 days	0.87	0.996	35.3	6.05	0.611	4.53	12.97	0.818	2.10
4 days	0.87	0.997	82.0	5.02	0.636	5.32	12.23	0.836	2.08
7 days	0.88	0.997	25.3	7.16	0.624	3.00	13.78	0.875	1.69
10 days	0.90	0.997	21.2	8.58	0.626	2.04	11.59	0.851	1.51
17 days	0.96	0.996	18.6	11.49	0.623	1.00	8.02	0.800	1.53

In more detail,  $\text{Ce}^{3+}$  ions present in the Si/Zr-based hybrid sol-gel coating can be released in the vicinity of the coating's defect. Due to the pH increase by the oxygen reduction reaction and  $\text{OH}^-$  ion release, the precipitation of cerium oxide/hydroxide at the Al substrate takes place at cathodic sites [59]. Since these precipitates hinder the flux of electrons from the anodic areas to new developing cathodic places, the cathodic reactions are hindered, and consequently, the anodic activity vanishes [59].

The inhibiting effect of  $\text{Ce}^{3+}$  ions can be attributed to the cerium oxide/hydroxide blocking effect in the pinholes of the TMZ-3 coating, i.e., to the self-healing effect. This effect was observed in increased  $R_p$  values obtained after four days of immersion (Figure 8b). Additionally, this effect was also suggested by long-term measurements of  $E_{oc}$  vs. time (Figure 4).

The beneficial effect of Ce-doping is especially pronounced after longer immersion times. EIS spectra and impedance parameters of both TMZ-3 and TMZ-3-Ce coatings demonstrate a good protection level of the underlying aluminum substrate over several days of immersion testing in chloride-containing environments. The presence of an intermediate oxide layer combined with the Si–O–Si and Si–O–Zr structure within the coatings supports corrosion resistance in chloride-containing electrolyte (see  $R_{oxide}$  values in Table 3). The protection level is dependent on the immersion time. Although the decrease of the  $|Z|$ ,  $R_{oxide}$  and  $R_{ct}$  values was observed (Figures 5 and 6 and Table 3), the  $R_p$  values maintained in the  $\text{M}\Omega \text{ cm}^2$  range during seven days of NaCl exposure. The faster degradation of the non-doped hybrid coating occurs probably due to the hydrolysis of the polysiloxane network and the formation of  $\text{Si}(\text{OH})_4$  [60]. On the other hand, Ce-doped coatings exhibit higher Al–O–Si/Zr bond density across the coating, which imparts a longer durability in chloride solution, even up to 17 days (Figures 6 and 8).

#### 4. Conclusions

- Hybrid Si/Zr sol-gel coatings with three different contents of Zr (0.06, 0.12 and 0.48 mol) without and with the addition of  $\text{Ce}^{3+}$  ions (0.5 wt. %  $\text{Ce}(\text{NO}_3)_3$ ) were synthesized for the protection of aluminum against corrosion in 0.1 M NaCl. These sol-gel coatings were denoted TMZ-1, TMZ-2, TMZ-3, TMZ-1-Ce, TMZ-2-Ce and TMZ-3-Ce, respectively.
- According to the results of Raman spectroscopy, photothermal beam deflection spectroscopy and electrochemical techniques, TMZ-3 and Ce-doped TMZ-3-Ce coatings, containing the highest Zr content, exhibit structural homogeneity and decreased porosity. Hence, excellent protecting properties and corrosion resistance were imparted to the underlying aluminum substrate. Corrosion current density,  $j_{corr}$ , decreased for two orders of magnitude in comparison to the uncoated Al substrate (see Table 2).
- The beneficial effect of the Ce-doping on the coating's protection properties was more pronounced upon long-lasting immersion of coated aluminum samples in 0.1 M NaCl. The excellent barrier properties and long-lasting anticorrosive protection properties of Ce-doped coatings

were related to the combined effect of a more condensed Si–O–Zr network structure and the passivating/inhibiting effect of Ce<sup>3+</sup> ions. The synergism between Zr and Ce ions integrated in the coating structure results in a simultaneous dual action of Ce ions: in the coating's self-healing process as inhibiting agents and in producing an effective anticorrosive barrier to the underlying Al substrate.

### List of Abbreviations

AA7075-T6	aluminum alloy 7075-T6
AFM	atomic force microscopy
CNLS	the complex non-linear least squares fit analysis software
CPE	constant phase element
DLS	dynamic light scattering
EEC	electric equivalent circuit
EIS	electrochemical impedance spectroscopy
EDS	energy dispersive X-ray spectrometry
FTIR	Fourier transform infrared spectroscopy
GDOES	glow discharge optimal emission spectroscopy
MAA	methacrylic acid, H <sub>2</sub> C=C(CH <sub>3</sub> )COOH
MAPTMS	3-methacryloxypropyltrimethoxy silane, H <sub>2</sub> C=C(CH <sub>3</sub> )CO <sub>2</sub> (CH <sub>2</sub> ) <sub>3</sub> Si(OCH <sub>3</sub> ) <sub>3</sub>
NMR	nuclear magnetic resonance spectroscopy
PBD	photothermal beam deflection spectroscopy
SEM	scanning electron spectroscopy
TEOS	tetraethyl orthosilicate, Si(OC <sub>2</sub> H <sub>5</sub> ) <sub>4</sub>
TG	temperature gradient
TGA	thermogravimetric analysis
TMZ	Si/Zr-based hybrid sol-gel coatings
TMZ-Ce	Ce-doped Si/Zr-based hybrid sol-gel coatings
ZTP	zirconium tetrapropoxide, Zr(OCH <sub>2</sub> CH <sub>2</sub> CH <sub>3</sub> ) <sub>4</sub>

### List of Symbols

$D_0$	thermal diffusivity of material without cavities (m <sup>2</sup> /s)
$D_s$	thermal diffusivity of porous material (m <sup>2</sup> /s)
$dE/dt$	potential scan rate (V·s <sup>-1</sup> )
$E$	potential (V)
$E_{\text{corr}}$	corrosion potential (V)
$E_{\text{oc}}$	open circuit potential (V)
$f$	frequency (Hz)
$j$	current density (A·cm <sup>-2</sup> )
$j_{\text{corr}}$	corrosion current density (A·cm <sup>-2</sup> )
$j\omega$	complex variable for sinusoidal perturbations with $\omega = 2\pi f$
$k_0$	thermal conductivity of material without cavities (W/(m·K))
$k_s$	thermal conductivity of porous material (W/(m·K))
$n$	exponent of the constant phase element
$n_{\text{coat}}$	exponent of the constant phase element related to the coating
$n_{\text{dl}}$	exponent of the constant phase element related to the double layer capacitance
$n_{\text{oxide}}$	exponent of the constant phase element related to the intermediate oxide layer
$P$	coating porosity (%)
$Q$	frequency-independent real constant ( $\Omega^{-1}\cdot\text{cm}^{-2}\cdot\text{s}^n$ )
$Q_{\text{coat}}$	pseudo-capacitance of the film   electrolyte interface ( $\Omega^{-1}\cdot\text{cm}^{-2}\cdot\text{s}^n$ )
$Q_{\text{dl}}$	double layer interfacial capacitance ( $\Omega^{-1}\cdot\text{cm}^{-2}\cdot\text{s}^n$ )
$Q_{\text{oxide}}$	pseudo-capacitance of the intermediate oxide layer ( $\Omega^{-1}\cdot\text{cm}^{-2}\cdot\text{s}^n$ )
$R$	resistance ( $\Omega\cdot\text{cm}^2$ )

$R_{\text{coat}}$	coating resistance ( $\Omega \cdot \text{cm}^2$ )
$R_{\text{ct}}$	charge-transfer resistance describing the Faradaic reaction at the metal   electrolyte solution interface ( $\Omega \cdot \text{cm}^2$ )
$R_{\text{oxide}}$	resistance of the intermediate oxide layer ( $\Omega \cdot \text{cm}^2$ )
$R_{\text{p}}$	polarization resistance ( $\Omega \cdot \text{cm}^2$ )
$R_{\Omega}$	ohmic resistance ( $\Omega \cdot \text{cm}^2$ )
$Z$	impedance ( $\Omega \cdot \text{cm}^2$ )
$ Z $	impedance magnitude ( $\Omega \cdot \text{cm}^2$ )
Greek Letters	
$\gamma$	ratio of thermal conductivity of cavities to material

**Acknowledgments:** The authors acknowledge the financial support from the Slovenian Research Agency (research core funding Nos. P2-0393 and P1-0134, project “Lightweight alloys based on aluminum as materials with increasing potential in transport industry”, ID J1-6734, and the bilateral project between Slovenia and Argentina (BI-AR/12-14-010)). The authors thank Beatriz Valcarce of the INTEMA (CONICET) for valuable help during Raman analysis and Dolores Zimerl of the Jožef Stefan Institute for valuable technical help. Peter Rodič thanks the Talents<sup>3</sup> fellowship program managed by AREA Science Park, with the financial contribution of the Friuli Venezia Giulia Autonomous Region through the European Social Fund for the funding of his research stay at the University of Udine. This work is a part of the M-ERA.NET project entitled “Design of corrosion resistant coatings targeted for versatile applications” (acronym COR\_ID) financially supported by the Ministry of Education, Science and Sport of the Republic of Slovenia. The authors thank Matic Lozinšek of the Jožef Stefan Institute for critical reading of the manuscript.

**Author Contributions:** Peter Rodič and Ingrid Milošev synthesized the sols, prepared the specimens, performed the electrochemical measurements and wrote the majority of the paper as the first and corresponding author, respectively. The coauthors contributed to the evaluation and discussion on the following techniques employed in this study: Paula M. Desimone and Silvia M. Ceré, the Raman spectroscopy results; Dorota Korte and Mladen Franko, the results obtained by the photothermal beam deflection spectroscopy; Jozefina Katić and Mirjana Metikoš-Huković, the results obtained by electrochemical impedance spectroscopy.

**Conflicts of Interest:** The authors declare no conflict of interest.

## Appendix

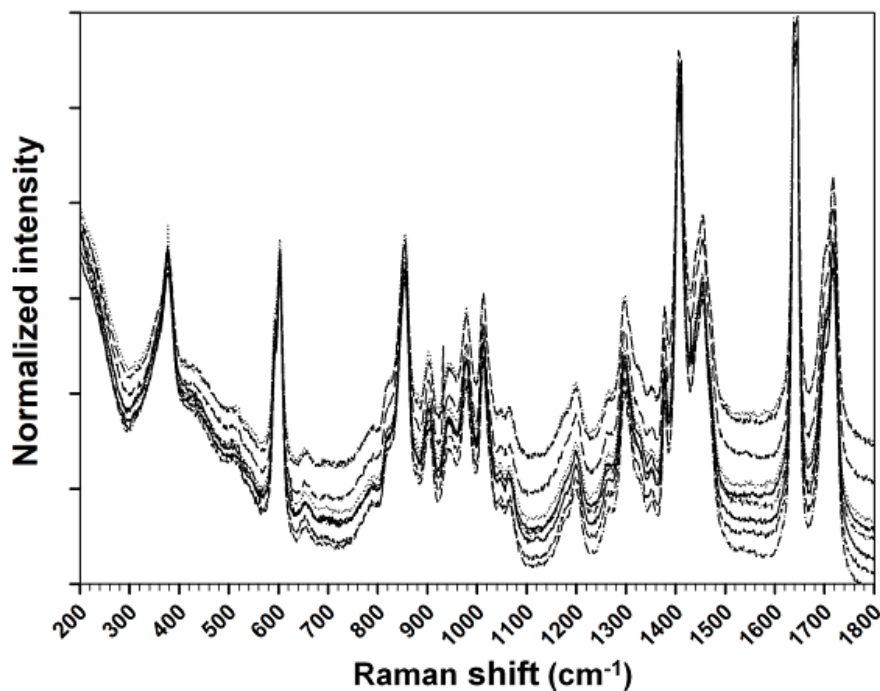


**Figure A1.** Linear scanning profile of Raman spectra recorded in the region that was 40  $\mu\text{m}$  wide with a 5  $\mu\text{m}$  step height for the TMZ-3 coating.

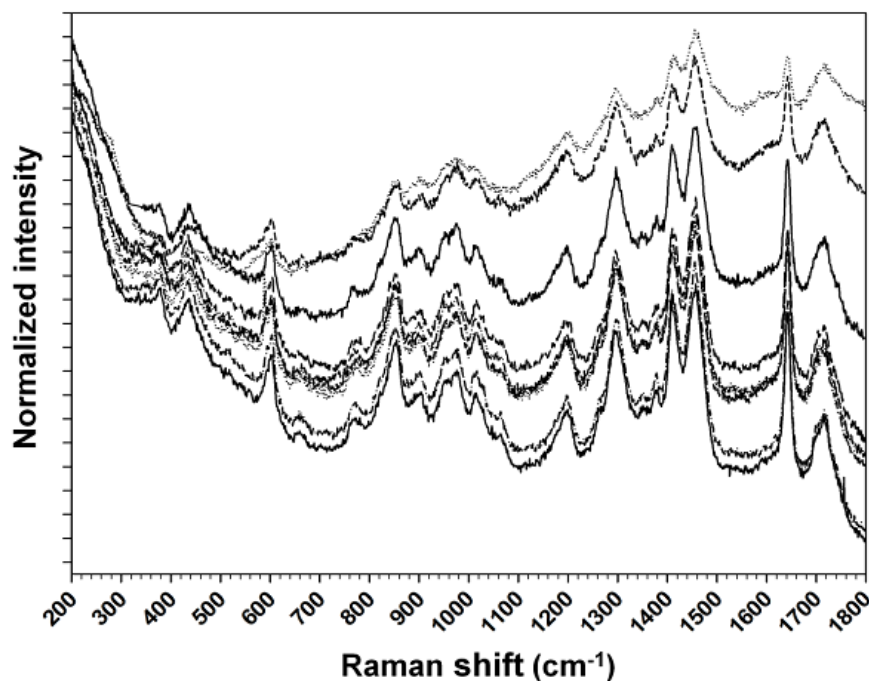


**Figure A2.** Linear scanning profile of Raman spectra recorded in the region that was 40  $\mu\text{m}$  wide with a 5- $\mu\text{m}$  step height for TMZ-3-Ce coating doped with 0.5 wt. % of  $\text{Ce}(\text{NO}_3)_3$ .

## References

1. Vargel, C. *Corrosion of Aluminium*, 2nd ed.; Elsevier: Kidlington, UK, 2004; ISBN 0 08 044495 4.
2. Zhao, J.; Xia, L.; Sehgal, A.; Lu, D.; McCreery, R.L.; Frankel, G.S. Effects of chromate and chromate conversion coatings on corrosion of aluminum alloy 2024-T3. *Surf. Coat. Technol.* **2001**, *140*, 51–57. [[CrossRef](#)]
3. Kendig, M.; Jeanjaquet, S.; Addison, R.; Waldrop, J. Role of hexavalent chromium in the inhibition of corrosion of aluminum alloys. *Surf. Coat. Technol.* **2001**, *140*, 58–66. [[CrossRef](#)]
4. ECHA European Chemicals Agency. ANNEX XVII TO REACH—Conditions of Restrictions. Entry 47—Chromium VI compounds. Available online: <https://echa.europa.eu/documents/10162/1f775bd4-b1b0-4847-937f-d6a37e2c0c98> (accessed on 4 April 2018).
5. VOC Solvents Emissions Directive—Environment—European Commission. Available online: <http://eur-lex.europa.eu/legal-content/EN/TXT/?uri=CELEX:31999L0013> (accessed on 7 November 2017).
6. Forsyth, M.; Seter, M.; Tan, M.Y.; Hinton, B. Recent developments in corrosion inhibitors based on rare earth metal compounds. *Corros. Eng. Sci. Technol.* **2014**, *49*, 130–135. [[CrossRef](#)]
7. Figueira, R.B.; Silva, C.J.R.; Pereira, E.V. Organic–inorganic hybrid sol–gel coatings for metal corrosion protection: A review of recent progress. *J. Coat. Technol. Res.* **2015**, *12*, 1–35. [[CrossRef](#)]
8. Abrahami, S.T.; de Kok, J.M.M.; Terryn, H.; Mol, J.M.C. Towards Cr(VI)-free anodization of aluminum alloys for aerospace adhesive bonding applications: A review. *Front. Chem. Sci. Eng.* **2017**, *11*, 465–482. [[CrossRef](#)]
9. Arkles, B. Commercial Applications of Sol-Gel-Derived Hybrid Materials. *MRS Bull.* **2001**, *26*, 402–408. [[CrossRef](#)]
10. Han, Y.-H.; Taylor, A.; Knowles, K.M. Scratch resistance and adherence of novel organic–inorganic hybrid coatings on metallic and non-metallic substrates. *Surf. Coat. Technol.* **2009**, *203*, 2871–2877. [[CrossRef](#)]
11. Andreeva, D.V.; Shchukin, D.G. Smart self-repairing protective coatings. *Mater. Today* **2008**, *11*, 24–30. [[CrossRef](#)]
12. Rodič, P.; Milošev, I.; Lekka, M.; Andreatta, F.; Fedrizzi, L. Corrosion behaviour and chemical stability of transparent hybrid sol-gel coatings deposited on aluminium in acidic and alkaline solutions. *Prog. Org. Coat.* Available online: <https://doi.org/10.1016/j.porgcoat.2018.02.025> (accessed on 22 March 2018).
13. Castro, Y.; Aparicio, M.; Moreno, R.; Duran, A. Silica-zirconia alkali-resistant coatings by sol-gel route. *J. Sol-Gel Sci. Technol.* **2005**, *35*, 41–50. [[CrossRef](#)]

14. Andreatta, F.; Paussa, L.; Lanzutti, A.; Rosero Navarro, N.C.; Aparicio, M.; Castro, Y.; Duran, A.; Ondratschek, D.; Fedrizzi, L. Development and industrial scale-up of ZrO<sub>2</sub> coatings and hybrid organic–inorganic coatings used as pre-treatments before painting aluminium alloys. *Prog. Org. Coat.* **2011**, *72*, 3–14. [[CrossRef](#)]
15. Wang, T.; Wang, X.; Zhang, Y.; Liu, L.; Xu, L.; Liu, Y.; Zhang, L.; Luo, Z.; Cen, K. Effect of zirconium(IV) propoxide concentration on the thermophysical properties of hybrid organic-inorganic films. *J. Appl. Phys.* **2008**, *104*, 013528. [[CrossRef](#)]
16. Rodič, P.; Iskra, J.; Milošev, I. A hybrid organic–inorganic sol–gel coating for protecting aluminium alloy 7075-T6 against corrosion in Harrison’s solution. *J. Sol-Gel Sci. Technol.* **2014**, *70*, 90–103. [[CrossRef](#)]
17. Rodič, P.; Iskra, J.; Milošev, I. Study of a sol–gel process in the preparation of hybrid coatings for corrosion protection using FTIR and <sup>1</sup>H NMR methods. *J. Non-Cryst. Solids* **2014**, *396–397*, 25–35. [[CrossRef](#)]
18. Rodič, P.; Mertelj, A.; Borovšak, M.; Benčan, A.; Mihailović, D.; Malič, B.; Milošev, I. Composition, structure and morphology of hybrid acrylate-based sol–gel coatings containing Si and Zr composed for protective applications. *Surf. Coat. Technol.* **2016**, *286*, 388–396. [[CrossRef](#)]
19. Rodič, P.; Milošev, I. Corrosion Properties of UV Cured Hybrid Sol-Gel Coatings on AA7075-T6 Determined under Simulated Aircraft Conditions. *J. Electrochem. Soc.* **2014**, *161*, C412–C420. [[CrossRef](#)]
20. Rodič, P.; Milošev, I. Electrochemical and Salt Spray Testing of Hybrid Coatings Based on Si and Zr Deposited on Aluminum and Its Alloys. *J. Electrochem. Soc.* **2015**, *162*, C592–C600. [[CrossRef](#)]
21. Varma, P.C.R.; Colreavy, J.; Cassidy, J.; Oubaha, M.; Duffy, B.; McDonagh, C. Effect of organic chelates on the performance of hybrid sol–gel coated AA 2024-T3 aluminium alloys. *Prog. Org. Coat.* **2009**, *66*, 406–411. [[CrossRef](#)]
22. Varma, P.C.R.; Colreavy, J.; Cassidy, J.; Oubaha, M.; McDonagh, C.; Duffy, B. Corrosion Protection of AA 2024-T3 Aluminium Alloys Using 3, 4-Diaminobenzoic Acid Chelated Zirconium-Silane Hybrid Sol-Gels. *Thin Solid Films* **2010**, *518*, 5753–5761. [[CrossRef](#)]
23. Varma, P.C.R.; Cassidy, J.; Oubaha, M.; McDonagh, C.; Colreavy, J.; Duffy, B. Corrosion Protection Properties of Various Ligand Modified Organic Inorganic Hybrid Coating on AA 2024-T3. *ECS Trans.* **2010**, *24*, 231–246. [[CrossRef](#)]
24. Paussa, L.; Navarro, N.C.R.; Bravin, D.; Andreatta, F.; Lanzutti, A.; Aparicio, M.; Durán, A.; Fedrizzi, L. ZrO<sub>2</sub> sol–gel pre-treatments doped with cerium nitrate for the corrosion protection of AA6060. *Prog. Org. Coat.* **2012**, *2*, 311–319. [[CrossRef](#)]
25. *Handbook of Smart Coatings for Materials Protection*; Makhlof, A.S.H. (Ed.) Woodhead Publishing Ltd.: Cambridge, UK, 2014; ISBN 0-85709-680-X.
26. Rosero-Navarro, N.C.; Figiel, P.; Jedrzejewski, R.; Biedunkiewicz, A.; Castro, Y.; Aparicio, M.; Pellice, S.A.; Durán, A. Influence of cerium concentration on the structure and properties of silica-methacrylate sol–gel coatings. *J. Sol-Gel Sci. Technol.* **2010**, *54*, 301–311. [[CrossRef](#)]
27. Druart, M.-E.; Recloux, I.; Thai, T.T.; Ershov, S.; Snyders, R.; Olivier, M.-G. Impact of the addition of cerium salts (Ce(III) and Ce(IV)) on formation and ageing of a silica sol-gel layer. *Surf. Coat. Technol.* **2016**, *304*, 40–50. [[CrossRef](#)]
28. Lakshmi, R.V.; Aruna, S.T.; Anandan, C.; Bera, P.; Sampath, S. EIS and XPS studies on the self-healing properties of Ce-modified silica-alumina hybrid coatings: Evidence for Ce(III) migration. *Surf. Coat. Technol.* **2017**, *309*, 363–370. [[CrossRef](#)]
29. Rodič, P.; Milošev, I. Corrosion Inhibition of Pure Aluminium and Alloys AA2024-T3 and AA7075-T6 by Cerium(III) and Cerium(IV) Salts. *J. Electrochem. Soc.* **2016**, *163*, C85–C93. [[CrossRef](#)]
30. Milošev, I.; Rodič, P. Cerium chloride and acetate salts as corrosion inhibitors for aluminium alloy AA7075-T6 in sodium chloride solution. *Corrosion* **2016**, *72*, 1021–1034. [[CrossRef](#)]
31. Volarič, B.; Milošev, I. Rare earth chloride and nitrate salts as individual and mixed inhibitors for aluminium alloy 7075-T6 in chloride solution. *Corros. Eng. Sci. Technol.* **2017**, *52*, 201–211. [[CrossRef](#)]
32. Andreatta, F.; Lohrengel, M.M.; Terryn, H.; de Wit, J.H.W. Electrochemical characterisation of aluminium AA7075-T6 and solution heat treated AA7075 using a micro-capillary cell. *Electrochimica Acta* **2003**, *48*, 3239–3247. [[CrossRef](#)]
33. Andreatta, F.; Druart, M.-E.; Lanzutti, A.; Lekka, M.; Cossement, D.; Olivier, M.-G.; Fedrizzi, L. Localized corrosion inhibition by cerium species on clad AA2024 aluminium alloy investigated by means of electrochemical micro-cell. *Corros. Sci.* **2012**, *65*, 376–386. [[CrossRef](#)]

34. Paussa, L.; Andreatta, F.; De Felicis, D.; Bemporad, E.; Fedrizzi, L. Investigation of AA2024-T3 surfaces modified by cerium compounds: A localized approach. *Corros. Sci.* **2014**, *78*, 215–222. [[CrossRef](#)]
35. Fontinha, I.R.; Salta, M.M.; Zheludkevich, M.L.; Ferreira, M.G.S.; Figueira, R.B.; Pereira, E.V.; Silva, C.J.R. Influence of pH on the Corrosion Protection of Epoxy-Silica-Zirconia Sol-Gel Coatings Applied on EN AW-6063 Aluminium Alloy. *ECS Trans.* **2014**, *58*, 9–16. [[CrossRef](#)]
36. Fedel, M.; Callone, E.; Fabbian, M.; Deflorian, F.; Dirè, S. Influence of Ce<sup>3+</sup> doping on molecular organization of Si-based organic/inorganic sol-gel layers for corrosion protection. *Appl. Surf. Sci.* **2017**, *414*, 82–91. [[CrossRef](#)]
37. Yu, M.; Liu, Y.; Liu, J.; Li, S.; Xue, B.; Zhang, Y.; Yin, X. Effects of cerium salts on corrosion behaviors of Si–Zr hybrid sol–gel coatings. *Chin. J. Aeronaut.* **2015**, *28*, 600–608. [[CrossRef](#)]
38. Cambon, J.-B.; Esteban, J.; Ansart, F.; Bonino, J.-P.; Turq, V.; Santagneli, S.H.; Santilli, C.V.; Pulcinelli, S.H. Effect of cerium on structure modifications of a hybrid sol–gel coating, its mechanical properties and anti-corrosion behavior. *Mater. Res. Bull.* **2012**, *47*, 3170–3176. [[CrossRef](#)]
39. Korte, D.; Franko, M. Application of complex geometrical optics to determination of thermal, transport, and optical parameters of thin films by the photothermal beam deflection technique. *J. Opt. Soc. Am. A* **2015**, *32*, 61–74. [[CrossRef](#)] [[PubMed](#)]
40. Pawlak, M.; Pal, S.; Ludwig, A.; Wieck, A.D. On the infrared absorption coefficient measurement of thick heavily Zn doped GaAs using spectrally resolved modulated photothermal infrared radiometry. *J. Appl. Phys.* **2017**, *122*, 229901. [[CrossRef](#)]
41. Chrobak, Ł.; Maliński, M.; Pawlak, M. Measurements of the optical absorption coefficient of Ar<sup>8+</sup> ion implanted silicon layers using the photothermal radiometry and the modulated free carrier absorption methods. *Infrared Phys. Technol.* **2014**, *67*, 604–608. [[CrossRef](#)]
42. Maliński, M.; Chrobak, Ł. Numerical analysis of absorption and transmission photoacoustic spectra of silicon samples with differently treated surfaces. *Opto-Electron. Rev.* **2011**, *19*, 46–50. [[CrossRef](#)]
43. Boukamp, B.A. A Nonlinear Least Squares Fit procedure for analysis of immittance data of electrochemical systems. *Solid State Ion.* **1986**, *20*, 31–44. [[CrossRef](#)]
44. Brug, G.J.; van den Eeden, A.L.G.; Sluyters-Rehbach, M.; Sluyters, J.H. The analysis of electrode impedances complicated by the presence of a constant phase element. *J. Electroanal. Chem. Interfacial Electrochem.* **1984**, *176*, 275–295. [[CrossRef](#)]
45. Jorcin, J.-B.; Orazem, M.E.; Pébère, N.; Tribollet, B. CPE analysis by local electrochemical impedance spectroscopy. *Electrochimica Acta* **2006**, *51*, 1473–1479. [[CrossRef](#)]
46. Lasia, A. Electrochemical Impedance Spectroscopy and its Applications. In *Modern Aspects of Electrochemistry*; Conway, B.E., Bockris, J.O., White, R.E., Eds.; Springer: Boston, MA, USA, 2002; Volume 32, pp. 143–248, ISBN 978-0-306-45964-1.
47. McMillan, P. Structural studies of silicate glasses and melts-applications and limitations of Raman spectroscopy. *Am. Mineral.* **1984**, *69*, 622–644.
48. Kalampounias, A.G. IR and Raman spectroscopic studies of sol–gel derived alkaline-earth silicate glasses. *Bull. Mater. Sci.* **2011**, *34*, 299–303. [[CrossRef](#)]
49. Zheludkevich, M.L.; Serra, R.; Montemor, M.F.; Salvado, I.M.M.; Ferreira, M.G.S. Corrosion protective properties of nanostructured sol–gel hybrid coatings to AA2024-T3. *Surf. Coat. Technol.* **2006**, *200*, 3084–3094. [[CrossRef](#)]
50. Araújo, V.D.; Avansi, W.; de Carvalho, H.B.; Moreira, M.L.; Longo, E.; Ribeiro, C.; Bernardi, M.I.B. CeO<sub>2</sub> nanoparticles synthesized by a microwave-assisted hydrothermal method: evolution from nanospheres to nanorods. *CrystEngComm* **2012**, *14*, 1150–1154. [[CrossRef](#)]
51. Silva, I.d.C.; Sigoli, F.A.; Mazali, I.O. Reversible Oxygen Vacancy Generation on Pure CeO<sub>2</sub> Nanorods Evaluated by in Situ Raman Spectroscopy. *J. Phys. Chem. C* **2017**, *121*, 12928–12935. [[CrossRef](#)]
52. Assefa, Z.; Haire, R.G.; Caulder, D.L.; Shuh, D.K. Correlation of the oxidation state of cerium in sol-gel glasses as a function of thermal treatment via optical spectroscopy and XANES studies. *Spectrochim. Acta Part A Mol. Biomol. Spectrosc.* **2004**, *60*, 1873–1881. [[CrossRef](#)] [[PubMed](#)]
53. Hinton, B.R.W.; Arnott, D.R.; Ryan, N.E. The inhibition of aluminium alloy corrosion by cerous cations. *Met. Forum* **1984**, *7*, 211–217.
54. Abdollah Zadeh, M.; van der Zwaag, S.; Garcia, S.J. Routes to extrinsic and intrinsic self-healing corrosion protective sol-gel coatings: A review. *Self-Heal. Mater.* **2013**, *1*, 1–18. [[CrossRef](#)]

55. Scully, J.R. Polarization Resistance Method for Determination of Instantaneous Corrosion Rates. *Corrosion* **2000**, *56*, 199–218. [[CrossRef](#)]
56. Mansfeld, F. Fundamental aspects of the polarization resistance technique—the early days. *J. Solid State Electrochem.* **2009**, *13*, 515–520. [[CrossRef](#)]
57. Zheludkevich, M.L.; Yasakau, K.A.; Bastos, A.C.; Karavai, O.V.; Ferreira, M.G.S. On the application of electrochemical impedance spectroscopy to study the self-healing properties of protective coatings. *Electrochem. Commun.* **2007**, *9*, 2622–2628. [[CrossRef](#)]
58. Santana, I.; Pepe, A.; Jimenez-Pique, E.; Pellice, S.; Milošev, I.; Ceré, S. Corrosion protection of carbon steel by silica-based hybrid coatings containing cerium salts: Effect of silica nanoparticle content. *Surf. Coat. Technol.* **2015**, *265*, 106–116. [[CrossRef](#)]
59. Trabelsi, W.; Cecilio, P.; Ferreira, M.G.S.; Montemor, M.F. Electrochemical assessment of the self-healing properties of Ce-doped silane solutions for the pre-treatment of galvanised steel substrates. *Prog. Org. Coat.* **2005**, *54*, 276–284. [[CrossRef](#)]
60. Juan-Díaz, M.J.; Martínez-Ibáñez, M.; Hernández-Escolano, M.; Cabedo, L.; Izquierdo, R.; Suay, J.; Gurruchaga, M.; Goñi, I. Study of the degradation of hybrid sol-gel coatings in aqueous medium. *Prog. Org. Coat.* **2014**, *77*, 1799–1806. [[CrossRef](#)]



© 2018 by the authors. Licensee MDPI, Basel, Switzerland. This article is an open access article distributed under the terms and conditions of the Creative Commons Attribution (CC BY) license (<http://creativecommons.org/licenses/by/4.0/>).